Metal dissolution from first principles: Potential-dependent kinetics and charge transfer

Shubham Sharma [a,*], Alexandra Zagalskaya [b], Stephen E. Weitzner [a], Lisa Eggart [c], Seongkoo Cho [a], Tim Hsu [a], Xiao Chen [a], Joel B. Varley [a], Vitaly Alexandrov [a], Christine A. Orme [a], Tuan Anh Pham [a], Brandon C. Wood [a]

[a] *Lawrence Livermore National Laboratory, Livermore, CA 94550, USA*
[b] *Department of Chemical and Biomolecular Engineering, University of Nebraska-Lincoln, Lincoln, NE, 68588, USA*
[c] *Michigan Technological University, Houghton, MI 49931, USA*

A B S T R A C T

Metal dissolution and its inverse process are integral to both corrosion and electrodeposition; however, many mechanistic details regarding the dissolution process are challenging to decipher. These include how ion dissolution kinetics and charge transfer are influenced by the competition between metal and solvent interactions under an electrode potential. In this work, we introduce a computational framework based on density functional theory with grand-canonical treatment of electrons to directly predict the potential energy landscape for metal dissolution at a constant potential. Using aluminum as an example, we demonstrate that dissolution kinetics is governed by competing kinetics between two physical processes associated with metal–metal bond breaking and ion-migration within the electrical double layer, respectively. We identify a kinetic transition between regimes dominated by each of these processes and show that this transition depends on the operating electrode potential, among other key factors. It is further found that kinetics and thermodynamics of these processes can be described with a simple, one-parameter Marcus-theory-type model. Beyond offering new understanding of charge transfer during dissolution, our simulation protocol provides a recipe for directly predicting other important quantities in electrochemical reactions from first principles that are difficult to measure, such as the symmetry factor.

1. Introduction

Predicting and controlling metal dissolution is critical for a broad array of applications, from corrosion and electrodeposition to development of electrochemical energy systems. In these applications, dissolution kinetics is often an important parameter that determine key performance metrics, such as the corrosion rate of alloys in aqueous environments, [1] and stability of electrode materials in ion batteries [2,3] and fuel cells [4]. From an activity point of view, it has also been demonstrated that dissolution of surface atoms in electrocatalysts may lower the overpotential for hydrogen production, pointing to the infamous trade-off between stability and activity in these materials [5, 6].

Experimentally, the thermodynamics of metal dissolution are well documented in terms of redox potentials; [7] however, the kinetics of these processes are far more challenging to measure and unravel.[8,9] Metal dissolution is notoriously complex, involving processes that are often competing and multiscale in nature. These include metal–metal bond breaking, formation of an ion solvation shell, and migration of the dissolved ion across the electrical double layer (EDL). This is further complicated by the fact that charge transfer accompanies dissolution,

meaning both electronic and ionic contributions synergistically determine the dissolution energetics and the associated mechanism. For electrochemical systems relevant for energy storage and conversion, electrode materials are also subjected to an external voltage, which can magnify the driving force for dissolution [10–12]. Under open-circuit conditions, such as those that commonly accompany corrosion, intrinsic potential gradients can play an analogous role [13]. As a result, dissolution kinetics depend both on the bias potential and the intrinsic reduction potential. Additional factors, such as surface orientation and defects, as well as solvent composition, further influence dissolution kinetics.

Some critical issues in understanding metal dissolution kinetics have been discussed by Gileadi [14]. One of the central questions regards the evolution of the metal charge state and hydration shell as the metal atom migrates from the substrate to the bulk solution during dissolution. A related question is how activation barriers are dictated by the competition between metal–metal and metal–solvent interactions. In addition, a detailed mechanistic understanding of the kinetically limiting step that governs the overall dissolution process is largely lacking, particularly under an applied potential. This can be

---

* Corresponding author.

E-mail addresses: sharma13@llnl.gov (S. Sharma), pham16@llnl.gov (T.A. Pham), wood37@llnl.gov (B.C. Wood).

attributed to the lack of experimental probes with sufficient resolution and sensitivity to isolate the highly complex dissolution process.

Atomistic simulations can aid with detailed understanding of dissolution; however, several technical challenges remain. Most atomistic studies have focused on reproducing the thermodynamics of dissolution. Early theoretical investigations combined empirical embedded atom (EAM) potentials and stochastic dynamics to simulate deposition of silver and platinum on a gold surface at specific electrode potentials [15]. Along similar lines, EAM variable charge-potentials were developed to provide a more realistic description of metal oxidation charge states during dissolution [16]. While providing important insights, these studies did not explicitly account for the metal–metal bond breaking and ion hydration formation [17]. With recent advancements in electronic structure methods, several attempts have been made to model metal dissolution or electrodeposition using first-principles approaches. For example, density functional theory (DFT) calculations were employed to predict trends in the thermodynamics of surface alloy dissolution in acidic media [18]. Another study combined DFT with the Effective Screening Medium (ESM) approach to compute free corrosion potentials, although assumptions were introduced to account for the kinetic terms [19]. By contrast, few attempts have been made to directly compute kinetics. Most notably, Taylor et al. used DFT to study dissolution kinetics of Cu and Ni–Cr alloy surfaces in liquid water [20, 21]. Although these studies directly accounted for the metal–metal bond breaking and ion hydration formation, the effects of constant electrode potential – a critical control knob in experimental setups – were not explicitly included. In another direction, Pinto and co-workers proposed a method that combines a model Hamiltonian, DFT and classical molecular dynamics (MD) simulations to predict dissolution kinetics for a series of monovalent and divalent metal ions [22,23]. Within this approach, the electronic and solvent contributions to the model Hamiltonian are derived separately using input parameters computed from DFT and force field simulations, respectively. More recently, Ma et al. developed an approach to predict the anisotropic anodic dissolution for metals, where the activation energy for dissolution is approximated through properties that are more straightforward to compute from first principles, including the surface energy density and work function [24].

Built on these studies, we present an alternative framework for directly evaluating the kinetics of metal dissolution from first principles under potentiostatic conditions that mimic realistic experimental setups. The approach is applied to elucidate previously unreported aspects of dissolution of an aluminum surface. We choose to study aluminum due to its importance in a wide range of technology and we expect that our study would present a baseline for understanding more realistic aluminum alloys. We show that aluminum dissolution is a double-barrier process, with the rate-limiting step switching between metal–metal bond breaking and ion migration across the EDL depending on the potential. Moreover, we discover that activation barriers associated with dissolution at a constant potential follow a quadratic and linear relationships with intermediate and large driving forces, respectively, and these relationships can be expressed with a single parameter that is functionally similar to a Marcus-theory type model. The computational framework also enables prediction of the symmetry factor governing macroscale reaction kinetics, which is found to be dependent on the potential energy difference between intermediate reaction steps as well as the bias.

2. Computational methods

Throughout this work, we consider an oxide-free aluminum (Al) surface, which is particularly relevant for understanding corrosion under low pH conditions or in crevices where solution mass transport is inhibited [25–27]. All calculations were carried out using DFT implemented in the Grid-Based Projector Augmented Wave (GPAW) code with a real-space grid basis set [28,29]. The Perdew–Burke–Ernzerhof (PBE) [30] exchange–correlation functional was employed with a real

grid spacing of 0.18 Å, and an optimized lattice constant of $a = 4.03$ Å was used. The lattice constant optimization was performed with a $21 \times 21 \times 21$ k-point mesh while a $4 \times 4 \times 1$ mesh was used for the surface calculations. In addition, we chose to study the common Al(111) surface, which was modeled with a $3 \times 3 \times 3$ slab where the bottom-most layer of the slab was constrained in the bulk position. A distance of at least 50 Å was used between the periodic images of the slab in the direction normal to the surface. Atomic manipulations and visualizations were handled using the Atomic Simulation Environment (ASE) [31].

Constant potential (*i.e.*, grand-canonical) surface calculations were performed using the Solvated Jellium Method (SJM), which allows selective charging of the unit cell while maintaining charge neutrality by adding a localized jellium counter charge in the implicit solvent region of the cell [32]. This method naturally localizes the excess charge only on the reactive side of the electrode, avoids spurious solvation effects, and solves the generalized Poisson equation to deduce the electrostatics. A dipole correction [33] is located between the jellium counter charge and the reverse of the periodic slab to isolate this counter charge and eliminate field effects on the reactive side. Energies for isolated systems, such as water molecules and $[Al(H_2O)_n]^{3+}$ clusters that represent the solvation shell of the Al^{3+} ion, were performed using conventional canonical DFT with a constant charge of 0 and + 3, respectively. For consistency, an implicit solvent scheme developed by Walter and Held was applied in all calculations except for in the case of bulk Al [34]. A dielectric constant, $\epsilon = 78.36$ and cavity shape parameter, $u_0 = 0.18$ eV was employed for describing the implicit water as provided in Ref. [34]. In all calculations, thermal (vibrational) contributions to the free energy where omitted. However, since the potential dependence of G (*i.e.*, Gibbs free energy) is reflected in the potential energy, we do not expect a significant change in the observed trends.

It is necessary to emphasize that there are several approaches besides SJM that have been developed over the years which treat charged electrochemical interfaces under constant potential conditions [35]. These can be broadly divided in to two categories *i.e.*, canonical and grand-canonical methods. With canonical approaches, the reaction energetics are performed using conventional DFT using finite size unit cells that are extrapolated to the constant-potential limit through a cell-extrapolation [36,37] scheme or using charge-extrapolation using interfacial capacitor models [38,39]. Although relatively simple, these extrapolation schemes are limited by the high computational cost associated with increasing cell size or the accuracy of charge partitioning methodologies. Relatively more sophisticated, grand-canonical [32,40–44] schemes, on the other hand, allow for explicit control of the electrode potential by allowing direct *charging* of the electrode interface while still maintaining charge neutrality to circumvent divergence issues for periodically repeated unit cells. Besides, explicit charging, most of the grand-canonical methods employ hybrid or continuum-solvation schemes that provide for adequate solvation as well as electrostatic *screening* effects resulting in a realistic representation of the EDL. The *charging* and *screening* schemes differ between implementations, but the unifying feature is to create a charge-compensating electrolyte which results in a charge neutral unit cell with a realistic electrostatic profile that mimics the EDL. Such charge-compensating electrolytes can be broadly classified into two categories: (i) localized *i.e.*, Gaussian-shaped [45,46] or spatially constrained, solvent-immersed counter charges (as implemented in SJM), and (ii) Boltzmann-weighted counter-ion distributions based on Poisson–Boltzmann (PB) equation [42,47]. Although less realistic than the PB approach, the appeal of SJM lies in its efficiency and stability for treating the electrostatic problem; for example, the generalized Poisson equation only needs to be solved once per self-consistent field step in SJM. By construct, the primary purpose of the implicit solvent in SJM is to provide a medium to generate a reasonable electrostatic profile
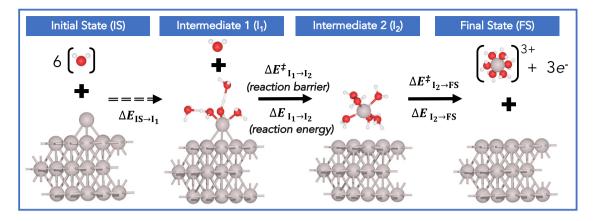
Fig. 1. Schematic of atom-by-atom dissolution from the Al(111) surface, with the example shown for an initial adatom. The dissolution reaction can be divided into two steps: (i) breaking metal–metal bonds and forming a full ion solvation ($I_1 \rightarrow I_2$); and (ii) ion migration into the bulk solution ($I_2 \rightarrow FS$). Thermodynamic driving force for dissolution is defined as the reaction energy associated with the transition of an Al atom initially in the solid phase (IS) to an Al^{3+} ion immersed in the solvent (FS). For completeness, thermodynamic difference between IS and I_1 states is also included.

rather than providing solvation effects to the system for which more sophisticated implicit/hybrid solvation models should be considered [32]. In its current form, the implicit solvent scheme by Walter and Held [34] have a solvation Gibbs energy accuracy of approx. 5 and 13 kJ/mol for neutral molecules and cations, respectively, which is comparable to some of the other continuum solvation models [48,49]. However, it is not recommended to apply the model to anions in water without further modification as short-range interactions between anions and water are not well represented. As we describe below, the inclusion of explicit water molecules in the first ion solvation shell is critical to achieve a good accuracy of dissolution energetics.

3. Results and discussions

Fig. 1 shows schematically how the atom-by-atom dissolution process proceeds from an intact Al(111) surface to a solvated Al^{3+} aqua complex. Using an adatom as an example, the dissolution process can be divided into two steps: (i) breaking of metal–metal bonds and formation of a full ion solvation, denoted by the reaction $I_1 \rightarrow I_2$; and (ii) ion migration into the bulk solution through the EDL, denoted by $I_2 \rightarrow FS$. The dissolution kinetics are determined by the evolution of this process, whereas the thermodynamic driving force for dissolution can be defined as the total reaction energy associated with the transition of an Al atom in the solid phase (IS) to an Al^{3+} ion immersed in the solvent (FS).

Before proceeding to study the surface and its associated kinetics, we first calculate the Al/Al^{3+} redox potential, which provides a convenient reference to validate our simulated results. The potential was computed by evaluating the reaction energy associated with the transition of an atom in the interior of bulk metal to an Al^{3+} aqua ion complex immersed in the solvent, accompanied by three electrons transferred to the metal (see Supporting Information). We obtain a value of -1.48 V_{SHE} for the redox potential, in reasonable agreement with the experimental value of -1.68 V_{SHE}. [7] We point out that a purely implicit solvation model is not sufficient to accurately describe the solvated ion. [50]. For example, as illustrated in Fig. 2A and Figure S1, employing just a single explicit water molecule along with an implicit solvent model leads to a redox potential of $+2.09$ V_{SHE}, which is drastically higher than the experimental number. The discrepancy is largely corrected when the solvated ion is instead described using the $[Al(H_2O)_n]^{3+}$ cluster with six explicit water molecules that form a complete solvation shell [51]. This confirms that our approach that combines six explicit water molecules forming the first hydration shell along with implicit solvation can be reasonably used for assessing dissolution energetics of the metal. We note that agreement with experiment would likely be further improved by including explicit water
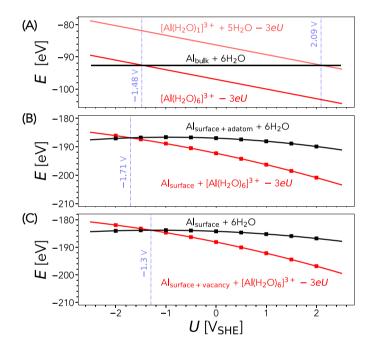

Fig. 2. Dissolution reaction energies for (A) an atom in bulk Al, (B) an adatom on the Al(111) surface, and (C) an atom on the pristine Al(111) surface. The point of intersection between the black (initial state) and red lines (final state) represents the Al/Al^{3+} redox potential. For (A), the initial state is a bulk-phase atom, whereas the final state is a solvated ion in the implicit solvent with a specific number of explicit water molecules. For (B) and (C), the solvated ion is described by a complex with six explicit water molecules.

molecules in the second ion hydration shell, and by accounting for entropic and/or thermal effects in the simulation model.

The results in Fig. 2A focus on the Al/Al^{3+} redox potential as a bulk property. In practice, dissolution is a surface phenomenon that is locally determined by the chemical bonding of the dissolving atoms (Fig. 1). This in turn depends on multiple factors, such as surface orientation, the presence of grain boundaries and defects, and the specific solution environment. For example, it has been demonstrated that dissolution rates of Alloy 22 (nickel–chromium–molybdenum–tungsten–iron) scale inversely with the coordination number of surface atoms for a given grain orientation in aggressive acidic environments [52]. Motivated by this study, we further investigate redox potentials of Al atoms with different coordination numbers. We focus on the defect free single-crystalline Al(111) surface for simplicity, and consider dissolution of an
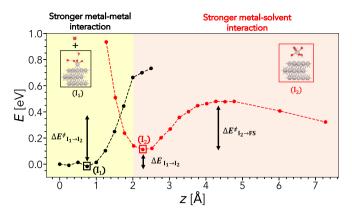
Fig. 3. Dissolution kinetics at -1 V_{SHE} as function of the distance (Z) between the adatom and the Al(111) surface. The black and red lines represent energies of the $I_1\big|_Z$ and $I_2\big|_Z$ configurations with varying positions of the $[Al(H_2O)_5]^{3+}$ and $[Al(H_2O)_6]^{3+}$ complexes, respectively. Definitions of the intermediate-stage barriers $\Delta E^{\ddagger}_{diss}$ and $\Delta E^{\ddagger}_{ion}$ are shown, along with the potential difference ΔE_{diss}. For $\Delta E^{\ddagger}_{diss}$, the barrier and transition state are determined by the intersection between the $I_1\big|_Z$ and $I_2\big|_Z$ potential energy profiles. The representative models of I_1 and I_2 show the local minimum energy structures along the $I_1\big|_Z$ and $I_1\big|_Z$ pathways, respectively. Shaded regions delineate qualitative dominance of metal–metal (yellow) versus metal–solvent (pink) interactions.

adatom and a surface atom that yield the lowest and highest possible coordination numbers, respectively (see Figure S2). Calculation of the redox potential of these species is shown in Fig. 2B & C. The potential was obtained by evaluating the difference in the energy between the initial state (IS) and the final state (FS) in Fig. 1. As expected, dissolving a surface adatom requires much less energy (by 0.41 V) than for the surface atom. The dissolution potentials of these two limiting cases – the adatom and surface atom – bound the value obtained for the bulk.

Beyond the Al/Al^{3+} redox potential, our simulation protocol can be extended to access kinetics of dissolution at a constant given potential. Here we focus on the adatom, shown in Fig. 1, as our limiting case of interest. The dissolution process can be intuitively separated into two reaction stages: breaking of metal–metal bonds and formation of a complete ion solvation ($I_1 \rightarrow I_2$); and migration of the ion–water complex to bulk solution through the EDL ($I_2 \rightarrow$ FS). Here, the I_1 state is modeled using five explicit water molecules that represent a partial solvation shell with an additional water molecule deep in the implicit solvent, whereas ion solvation of the I_2 state is modeled using six explicit water molecules. The I_1 and I_2 geometries represent the minimum energy structures on the potential energy wells obtained through incremental movement of $[Al(H_2O)_5]^{3+}$ and $[Al(H_2O)_6]^{3+}$ complexes represented by $I_1\big|_Z$ and $I_2\big|_Z$, respectively as shown in Fig. 3. The potential energy profiles of $I_1\big|_Z$ and $I_2\big|_Z$ along the surface normal were then obtained by varying the position of the $[Al(H_2O)_5]^{3+}$ and $[Al(H_2O)_6]^{3+}$ complexes in the presence of an applied potential. At each step, configurations of these complexes were optimized with the adatom fixed in the z-direction. The $I_1\big|_{Z=0}$ structure was obtained by optimizing the structure shown in Figure S3, where the adatom was not allowed to relax in the direction normal to the surface. The transition state and the corresponding reaction barrier ($\Delta E^{\ddagger}_{diss}$) associated with the $I_1 \rightarrow I_2$ step was approximated as the intersection between the potential energy profiles of $I_1\big|_Z$ and $I_2\big|_Z$ configurations. In this way, kinetics associated with temporary reconfiguration of the ion solvation due to the presence of the sixth water molecule is not included in our simulations. Finally, the transition state associated with $I_2 \rightarrow$ FS and the associated reaction barrier ($\Delta E^{\ddagger}_{ion}$) was obtained from the potential energy profile of $I_2\big|_Z$ as a function of distance from the surface. The grand-canonical potential energy landscape as a function of the distance of the metal adatom from the surface is shown in Fig. 3 for a representative applied potential of

-1 V_{SHE}. We note that a slow convergence of the energy of $I_2\big|_Z$ at a long distance is due to the electrostatic interaction between the $[Al(H_2O)_6]^{3+}$ complex and a charged electrode (see Figure S4) *i.e.*, it is dependent on the electrostatic potential. To mitigate this slow convergence and be thermodynamically consistent, the Final State (FS) of $I_2\big|_Z$ was obtained by treating the electrode and aqua-ion complex separately at constant potentials and constant charge of $+ 3$, respectively.

Following this simulation protocol, we carried out Bader charge analysis to elucidate the spatial evolution of the charge state of the dissolved metal. The charge state associated with the $I_1\big|_Z$ and $I_2\big|_Z$ geometries as functions of distance from the surface are shown in Fig. 4A & B, respectively. We find that the adatom (red lines) already exhibits cationic character with a charge state of around $+1.1$ in the $I_1\big|_{Z=0}$ configuration due to interactions with explicit waters and initial metal–metal bond stretching. As expected, the hydrated adatom becomes increasingly oxidized as the metal–metal bond continues to stretch until the bond is completely broken. The drop in the charge magnitude once the metal–metal bond breaks, shown in Fig. 4A, is an artifact of not accounting for the full six-water solvation shell when $I_1\big|_Z$ enters the solution. On the other hand, the Al adatom with a full first hydration shell in $I_2\big|_Z$ (Fig. 4B) yields a charge state of $+2$ when the ion complex transitions from the regime dominated by the metal–metal interaction to the one dominated by the metal–solvent interaction. This is an indication that as the metal dissolves, it evolves into the $+2$ state first before transitioning to the expected $+3$ state; the latter takes place as an outer-layer electron-transfer event as the metal ion migrates into the bulk solution. A lower charge state of the ion near the surface can be explained based on charge density analysis (Figure S5), which shows highly delocalized charge when the solvated ion is close to the metal surface, resulting in electron spilling from the surface to the metal ion. Our findings on the evolution of the charge state of the dissolved ion are consistent with Marcus theory, which suggests that dissolution of multivalent ions involves a series of one-electron steps as the required reorganization energy would be much higher for a simultaneous transfer of multiple electrons. Our results are also in agreement with the make-before break concept proposed by Gileadi, [14] who likewise concluded that the formation of the hydration shell would start when the effective charge of the ion is slightly cationic.

Our analysis also points to fundamentally different natures of the charge transfer reaction between dissolution and ion migration regimes, represented respectively by the $I_1\big|_Z$ and $I_2\big|_Z$ configurations. For the former, metal–metal bonds dominate the charge transfer, resulting in similar charge states for the dissolving metal center and for the cumulative hydrated metal-ion complex, as represented by the red and blue lines in Fig. 4A, respectively. On the other hand, because the ion is fully solvated in the I_2 configuration, the charge state of the metal-center remains stable at ≈ 2.6, whereas the rest of the charge in the solvated complex is delocalized across the surrounding water molecules (Fig. 4B). It is also found that it is the charge transfer between these water molecules and the metal surface that leads to the increase of the charge state of the entire ion complex to $+3$ as it migrates away from the surface.

The energetics of the entire dissolution process are summarized in Fig. 5. It is found that the reaction energy differences associated each step shown in Fig. 1 follow a simple linear relationship with respect to the applied potential (U). The slope of the each curve is the charge transfer associated with that step along the reaction coordinate, as obtained from SJM. For instance, the overall reaction from IS to FS yields a slope of ~ 3 (black line), consistent with a total of three electrons transferred during the entire Al dissolution process. Examination of the thermodynamic profiles reveals important additional findings. In particular, the transition from the Al adatom into a partially solvated ion (IS $\rightarrow$ I_1, magenta line) is always energetically
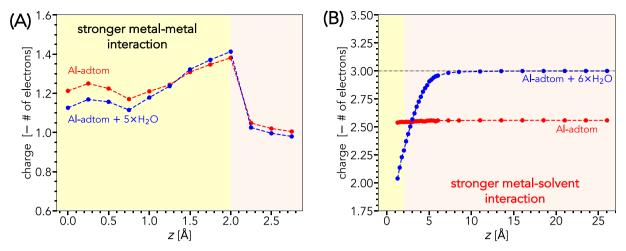
Fig. 4. Bader charge analysis at $-1\ V_{SHE}$ for the (A) $I_1\big|_Z$ and (B) $I_2\big|_Z$ configurations as function of distance (Z) between the adatom and the Al(111) surface. The red and blue lines represent the charge of just the metal center and of the entire metal–water complex, respectively. Shaded regions delineate qualitative dominance of metal–metal (yellow) versus metal–solvent (pink) interactions.
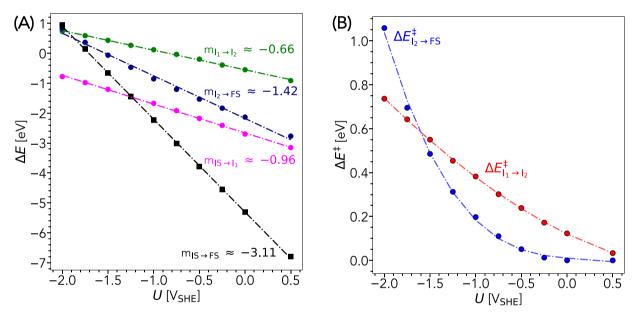

Fig. 5. Potential (U) dependence of (A) reaction energies and (B) reaction barriers for the steps highlighted in Fig. 1.

favorable. On the other hand, formation of a complete solvation shell by breaking the metal–metal bonds ($I_1 \rightarrow I_2$, green line) and migration of the solvated ion into the bulk solution through the EDL ($I_2 \rightarrow FS$, blue line) are thermodynamically unfavorable at very low potentials; they only become favorable around $-1.0\ V_{SHE}$ and $-1.5\ V_{SHE}$, respectively. Finally, it is shown that in the sampled potential range, the $I_1 \rightarrow I_2$ step is the most difficult during dissolution from a purely thermodynamic point of view.

The picture becomes more interesting when one also considers the impacts of kinetics. In particular, our simulations indicate that Al dissolution can be governed by either of two kinetically limiting processes, which are associated with metal–metal bond breaking and ion migration through the EDL (Fig. 5B, red and blue lines, respectively). In contrast to thermodynamics, kinetic barriers exhibit a more nonlinear behavior with respect to the potential. Specifically, we find that ion migration is the rate-limiting process at potentials lower than $-1.7\ V_{SHE}$, whereas the process of forming a complete ion solvation shell by breaking the metal–metal bond dominates at more positive

potentials. Collectively, these results indicate a complex dependence of dissolution kinetics on electrode potential, pointing to the importance of taking into account effects of potential bias in simulations involving electrochemical dissolution.

We further discuss the connection between results presented here and Marcus theory for predicting dissolution kinetics [53,54]. For each transition step, we consider the initial and final states to lie in a quadratic potential energy well (See Fig. 6A, inset), with the reaction barrier described by the point of intersection. This simple analytical model captures the basics of the dissolution process in limiting cases: as the reaction energy becomes strongly exothermic ($\Delta E \ll 0$), the reaction smoothly approaches an activationless state ($\Delta E^{\ddagger} \rightarrow 0$). Similarly, when the reaction becomes highly endothermic ($\Delta E \gg 0$), the kinetics are dominated by the large energy change of the reaction ($\Delta E^{\ddagger} \rightarrow \Delta E$), again indicating a barrierless reaction in this limit [55]. Intermediate cases involve a competition between kinetic and thermodynamic factors for determining the overall energy landscape. This
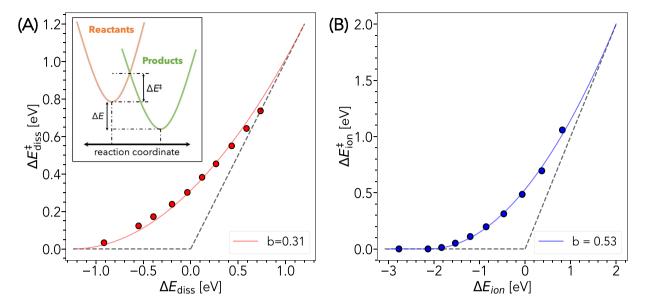
Fig. 6. Reaction energies and barriers of the dissolution (A) and ion-migration (B) reactions in the functional form described in Eq. (1). The relationship is quadratic for intermediate driving forces and linear for high magnitude driving forces. Inset of (A): Schematic showing reaction reactants and products to lie in the quadratic potential wells, and the reaction barrier is described by the point of intersection.

simple Marcus-theory-like relation can be described as:

$$\Delta E^{\ddagger} = \begin{cases} 0, & \Delta E < -4b \\ \frac{(\Delta E + 4b)^2}{16b}, & -4b \leq \Delta E \leq 4b \\ \Delta E, & \Delta E > 4b \end{cases} \tag{1}$$

where b can be interpreted as the intrinsic barrier, *i.e.*, the reaction barrier when the elementary step is thermoneutral ($\Delta E = 0$). As shown in Fig. 6, we find that relation between reaction energies and barriers of the two kinetically limiting processes of Al dissolution can be well captured with this simple one-parameter model. The limiting behavior is evident from the dissolution and ion-migration reactions (See Figs. 5B & 6); specifically, the reactions approach the barrierless and activation-less regions for highly negative and positive potentials, respectively. Overall, our analysis indicates that Marcus theory can be used for a qualitative description of the kinetics–thermodynamics relationship and evolution of the ion charge state of Al dissolution.

Beyond providing a detailed understanding of energetics and charge transfer reaction during Al dissolution, our simulation protocol can also be used to compute quantities that are not easily accessed by experimental probes. These include the symmetry factor (β), which is a key factor in the Butler–Volmer (BV) equation that has been largely employed for describing electrochemical reactions. The symmetry factor can be simply approximated as the rate of change of the activation energy with respect to the thermodynamic driving force for each of the electrochemical reactions:

$$\beta = \frac{d}{d\Delta E}\left(\Delta E^{\ddagger}\right) = \begin{cases} 0, & \Delta E < -4b \\ \frac{1}{2} + \frac{\Delta E}{8b}, & -4b \leq \Delta E \leq 4b \\ 1, & \Delta E > 4b \end{cases} \tag{2}$$

It can also be interpreted as the fractional charge transfer in the activation step of the electrochemical reactions. In practice, β is often assumed as 0.5 in the BV equation [56]. However, because our formalism gives a way of directly computing β for the two kinetically limiting processes of Al dissolution, we can assess and refine this approximation. Shown in Fig. 7, our results confirm that $\beta = 0.5$ is indeed a good approximation for the thermoneutral reaction under no applied bias. However, β can significantly deviate from 0.5 for driven reactions, such as those under an applied potential that often occur under operation. Moreover, our simulations indicate that symmetry factor is generally not identical across different electrochemical reaction steps. This is

indicated by the different slopes of β for the dissolution ($I_1 \rightarrow I_2$) and migration ($I_2 \rightarrow FS$) subprocesses discussed above. In particular, the migration step shows higher sensitivity of the symmetry factor to an applied bias, which reflects the particularly crucial role of the screened Coulomb interaction for determining the energy landscape for that process. Our analysis therefore indicates that the use of $\beta = 0.5$ for describing electrochemical processes must be practiced with care.

4. Conclusions

To conclude, we present a simple simulation protocol based on DFT with grand-canonical treatment of electrons to predict dissolution kinetics, charge transfer, and thermodynamics at constant bias potential. Applied to metallic Al as a demonstration case, our approach is used to show that Al dissolution can be governed by either of two potentially kinetically limiting processes. These processes are associated with metal–metal bond breaking and ion migration through the electric double layer. Interestingly, the limiting step switches depending on the applied potential. Our findings are generally consistent with a simple Marcus-theory type interpretation, particularly regarding the kinetics–thermodynamics relationship and nature of the charge transfer process during dissolution. Nevertheless, the simulations point to key subtleties that arise from driving the reaction under an applied bias. One critical example is the effect on the symmetry factor, which cautions use of the commonly used approximation of 0.5.

In addition to the specific findings presented here, the generality and flexibility of our approach enables extraction of analytical relationships between kinetics and thermodynamics for electrochemical dissolution and charge-transfer reactions. Our approach also offers a promising avenue to compute other important parameters, including the symmetry factor, from first-principles. Such relationships can be used to bridge connections to higher-order theories, such as those proposed by Ref. [24], for a more holistic treatment of electrochemical kinetics under different driving forces. It is also important to note that although we have focused solely on the defect-free Al(111) surface here, our method can be straightforwardly applied to study dissolution as a function of more complex surface factors, including surface orientation, point defects, grain boundaries, and impurities. Surfaces with step/kink edges, or those with preformed oxide films, can likewise be studied. Along these lines, work is underway to simulate dissolution of metal with an oxide layer for different pH conditions and ion types.
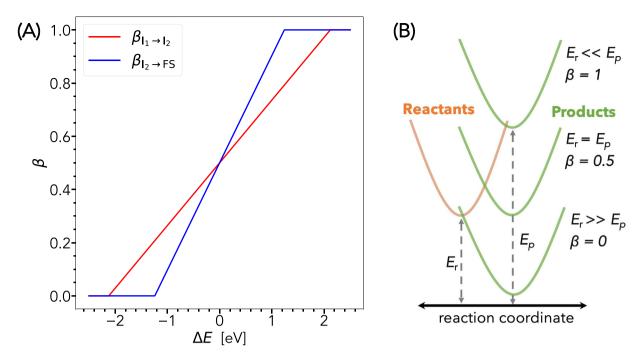
Fig. 7. (A) Symmetry factors computed as a function of applied potentials for the dissolution (red) and ion-diffusion processes (blue), and (B) Schematic showing the influence on the symmetry factor with varying energetics of an elementary step.

Looking forward, our simulation protocol can be used to elucidate the competition between oxide formation and metal dissolution, and to investigate how dissolution kinetics is governed by the interplay between interfacial chemistry, applied potentials, and solution chemistry. Finally, it is important to highlight some of the important factors that were beyond the scope of this study but could potentially influence dissolution kinetics. These include entropic effects, and kinetics associated with water transport and temporary reconfiguration of the ion solvation, which could be highly relevant within the context of Marcus theory. Similarly, additional efforts are required to understand how dissolution kinetics can be influenced by the choice of implicit solvation model as well as the number of explicit water molecules used to represent the ion solvation. A better understanding of the possible impact on dissolution energetics due to charge delocalization error [57] – a well-known issue in DFT – is highly desirable as the use of semi-local (GGA) exchange–correlation functionals like PBE could lead to overly dispersed charge distribution or nonphysical charge transfer at the interface.

CRediT authorship contribution statement

Shubham Sharma: Conceptualization, Methodology, Investigation, Formal analysis, Software, Writing – original draft. **Alexandra Zagalskaya:** Methodology. **Stephen E. Weitzner:** Methodology. **Lisa Eggart:** Writing – review & editing. **Seongkoo Cho:** Writing – review & editing. **Tim Hsu:** Writing – review & editing. **Xiao Chen:** Writing – review & editing. **Joel B. Varley:** Methodology, Validation. **Vitaly Alexandrov:** Writing – review & editing. **Christine A. Orme:** Writing – review & editing. **Tuan Anh Pham:** Supervision, Writing – original draft, Writing – review & editing. **Brandon C. Wood:** Supervision, Funding acquisition, Writing – review & editing.

Declaration of competing interest

The authors declare that they have no known competing financial interests or personal relationships that could have appeared to influence the work reported in this paper.

Data availability

Data will be made available on request.

Appendix A. Supplementary data

Supplementary material related to this article can be found online at https://doi.org/10.1016/j.electacta.2022.141443. Information regarding calculating dissolution/redox potential, generating intermediate structures, convergence of energy profile, and, analyzing charge density localization is provided in the Supporting Information.

References

[1] L.R. Faulkner, A.J. Bard, Electrochemical Methods: Fundamentals and Applications, John Wiley and Sons, 2002.

[2] D. Huang, C. Engtrakul, S. Nanayakkara, D.W. Mulder, S.-D. Han, M. Zhou, H. Luo, R.C. Tenent, Understanding degradation at the lithium-ion battery cathode/electrolyte interface: Connecting transition-metal dissolution mechanisms to electrolyte composition, ACS Appl. Mater. Interfaces 13 (10) (2021) 11930–11939.

[3] J.D. McBrayer, M.-T.F. Rodrigues, M.C. Schulze, D.P. Abraham, C.A. Apblett, I. Bloom, G.M. Carroll, A.M. Colclasure, C. Fang, K.L. Harrison, et al., Calendar aging of silicon-containing batteries, Nat. Energy 6 (9) (2021) 866–872.

[4] S. Cherevko, G.P. Keeley, S. Geiger, A.R. Zeradjanin, N. Hodnik, N. Kulyk, K.J.J. Mayrhofer, Dissolution of platinum in the operational range of fuel cells, ChemElectroChem 2 (10) (2015) 1471–1478.

[5] A. Zagalskaya, V. Alexandrov, Mechanistic study of IrO2 dissolution during the electrocatalytic oxygen evolution reaction, J. Phys. Chem. Lett. 11 (7) (2020) 2695–2700.

[6] A. Zagalskaya, V. Alexandrov, Role of defects in the interplay between adsorbate evolving and lattice oxygen mechanisms of the oxygen evolution reaction in RuO2 and IrO2, ACS Catal. 10 (6) (2020) 3650–3657.

[7] CRC Handbook, CRC Handbook of Chemistry and Physics, 88th Edition, 88th ed., CRC Press, 2007.

[8] D. Chu, R.F. Savinell, Experimental data on aluminum dissolution in KOH electrolytes, Electrochim. Acta 36 (10) (1991) 1631–1638.

[9] Z. Zhao, G. Frankel, Surface layer dissolution kinetics of aluminum alloy 7075 in various tempers, Corrosion 63 (7) (2007) 613–624.

[10] S. Sharma, C. Zeng, A.A. Peterson, Face-centered tetragonal (FCT) Fe and Co alloys of Pt as catalysts for the oxygen reduction reaction (ORR): A DFT study, J. Chem. Phys. 150 (4) (2019) 041704.

[11] J. Li, S. Sharma, K. Wei, Z. Chen, D. Morris, H. Lin, C. Zeng, M. Chi, Z. Yin, M. Muzzio, M. Shen, P. Zhang, A.A. Peterson, S. Sun, Anisotropic strain tuning of L10 ternary nanoparticles for oxygen reduction, J. Am. Chem. Soc. 142 (45) (2020) 19209–19216, PMID: 33124818.

[12] J. Li, S. Sharma, X. Liu, Y.-T. Pan, J.S. Spendelow, M. Chi, Y. Jia, P. Zhang, D.A. Cullen, Z. Xi, H. Lin, Z. Yin, B. Shen, M. Muzzio, C. Yu, Y.S. Kim, A.A. Peterson, K.L. More, H. Zhu, S. Sun, Hard-magnet L10-CoPt nanoparticles advance fuel cell catalysis, Joule 3 (1) (2019) 124–135.

[13] G. Frankel, N. Sridhar, Understanding localized corrosion, Mater. Today 11 (10) (2008) 38–44.

[14] E. Gileadi, The enigma of metal deposition, J. Electroanal. Soc. 660 (2) (2011) 247–253, Physics and Chemistry of Charge Transfer in Condensed Media.

[15] W. Schmickler, K. Pötting, M. Mariscal, A new simulation model for electrochemical metal deposition, Chem. Phys. 320 (2) (2006) 149–154.

[16] F.H. Streitz, J.W. Mintmire, Electrostatic potentials for metal-oxide surfaces and interfaces, Phys. Rev. B 50 (1994) 11996–12003.

[17] M.I. Baskes, S.G. Srinivasan, S.M. Valone, R.G. Hoagland, Multistate modified embedded atom method, Phys. Rev. B 75 (2007) 094113.

[18] J. Greeley, J.K. Nørskov, Electrochemical dissolution of surface alloys in acids: Thermodynamic trends from first-principles calculations, Electrochim. Acta 52 (19) (2007) 5829–5836.

[19] K. Kano, S. Hagiwara, T. Igarashi, M. Otani, Study on the free corrosion potential at an interface between an Al electrode and an acidic aqueous NaCl solution through density functional theory combined with the reference interaction site model, Electrochim. Acta 377 (2021) 138121.

[20] C.D. Taylor, The transition from metal–metal bonding to metal–solvent interactions during a dissolution event as assessed from electronic structure, Chem. Phys. Lett. 469 (1) (2009) 99–103.

[21] H. Ke, C.D. Taylor, DFT-based calculation of dissolution activation energy and kinetics of Ni–Cr alloys, J. Electrochem. Soc. 167 (13) (2020) 131508.

[22] L.M.C. Pinto, P. Quaino, E. Santos, W. Schmickler, On the Electrochemical Deposition and Dissolution of Divalent Metal Ions, ChemPhysChem 15 (1) (2014) 132–138.

[23] L.M.C. Pinto, E. Spohr, P. Quaino, E. Santos, W. Schmickler, Why Silver Deposition is so Fast: Solving the Enigma of Metal Deposition, Angew. Chem. Int. Ed. 52 (30) (2013) 7883–7885.

[24] H. Ma, X.-Q. Chen, R. Li, S. Wang, J. Dong, W. Ke, First-principles modeling of anisotropic anodic dissolution of metals and alloys in corrosive environments, Acta Mater. 130 (2017) 137–146.

[25] T. Bligaard, J.K. Nørskov, S. Dahl, J. Matthiesen, C.H. Christensen, J. Sehested, The Brønsted–Evans–Polanyi relation and the volcano curve in heterogeneous catalysis, J. Catal. 224 (1) (2004) 206–217.

[26] R.F. Reising, AC impedance studies of aluminum alloy 6061 in chloride solutions: The role of oxygen, hydrogen ions, and aluminum ions in initiating crevice corrosion, J. Electrochem. Soc. 134 (6) (1987) 1366–1374.

[27] A. Alavi, R. Cottis, The determination of pH, potential and chloride concentration in corroding crevices on 304 stainless steel and 7475 aluminium alloy, Corros. Sci. 27 (5) (1987) 443–451.

[28] J. Enkovaara, C. Rostgaard, J.J. Mortensen, J. Chen, M. Dułak, L. Ferrighi, J. Gavnholt, C. Glinsvad, V. Haikola, H.A. Hansen, H.H. Kristoffersen, M. Kuisma, A.H. Larsen, L. Lehtovaara, M. Ljungberg, O. Lopez-Acevedo, P.G. Moses, J. Ojanen, T. Olsen, V. Petzold, N.A. Romero, J. Stausholm-Møller, M. Strange, G.A. Tritsaris, M. Vanin, M. Walter, B. Hammer, H. Häkkinen, G.K.H. Madsen, R.M. Nieminen, J.K. Nørskov, M. Puska, T.T. Rantala, J. Schiøtz, K.S. Thygesen, K.W. Jacobsen, Electronic structure calculations with GPAW: a real-space implementation of the projector augmented-wave method, J. Phys.: Condens. Matter 22 (25) (2010) 253202, Publisher: IOP Publishing.

[29] J.J. Mortensen, L.B. Hansen, K.W. Jacobsen, Real-space grid implementation of the projector augmented wave method, Phys. Rev. B 71 (3) (2005) 035109, Publisher: American Physical Society.

[30] J.P. Perdew, K. Burke, M. Ernzerhof, Generalized gradient approximation made simple, Phys. Rev. Lett. 77 (18) (1996) 3865–3868, Publisher: American Physical Society.

[31] A.H. Larsen, J.J. Mortensen, J. Blomqvist, I.E. Castelli, R. Christensen, M. Dułak, J. Friis, M.N. Groves, B. Hammer, C. Hargus, E.D. Hermes, P.C. Jennings, P.B. Jensen, J. Kermode, J.R. Kitchin, E.L. Kolsbjerg, J. Kubal, K. Kaasbjerg, S. Lysgaard, J.B. Maronsson, T. Maxson, T. Olsen, L. Pastewka, A. Peterson, C. Rostgaard, J. Schiøtz, O. Schütt, M. Strange, K.S. Thygesen, T. Vegge, L. Vilhelmsen, M. Walter, Z. Zeng, K.W. Jacobsen, The atomic simulation environment—a Python library for working with atoms, J. Phys.: Condens. Matter 29 (27) (2017) 273002, Publisher: IOP Publishing.

[32] G. Kastlunger, P. Lindgren, A.A. Peterson, Controlled-potential simulation of elementary electrochemical reactions: Proton discharge on metal surfaces, J. Phys. Chem. C 122 (24) (2018) 12771–12781, Publisher: American Chemical Society.

[33] L. Bengtsson, Dipole correction for surface supercell calculations, Phys. Rev. B 59 (19) (1999) 12301–12304, Publisher: American Physical Society.

[34] A. Held, M. Walter, Simplified continuum solvent model with a smooth cavity based on volumetric data, J. Chem. Phys. 141 (17) (2014) 174108, Publisher: American Institute of Physics.

[35] N. Abidi, S.N. Steinmann, How are transition states modeled in heterogeneous electrocatalysis? Curr. Opin. Electrochem. 33 (2022) 100940.

[36] E. Skúlason, G.S. Karlberg, J. Rossmeisl, T. Bligaard, J. Greeley, H. Jónsson, J.K. Nørskov, Density functional theory calculations for the hydrogen evolution reaction in an electrochemical double layer on the Pt(111) electrode, Phys. Chem. Chem. Phys. 9 (2007) 3241–3250.

[37] E. Skúlason, V. Tripkovic, M.E. Björketun, S. Gudmundsdóttir, G. Karlberg, J. Rossmeisl, T. Bligaard, H. Jónsson, J.K. Nørskov, Modeling the electrochemical hydrogen oxidation and evolution reactions on the basis of density functional theory calculations, J. Phys. Chem. C 114 (42) (2010) 18182–18197.

[38] K. Chan, J.K. Nørskov, Potential dependence of electrochemical barriers from ab initio calculations, J. Phys. Chem. Lett. 7 (9) (2016) 1686–1690, PMID: 27088442.

[39] J.A. Gauthier, C.F. Dickens, S. Ringe, K. Chan, Practical considerations for continuum models applied to surface electrochemistry, ChemPhysChem 20 (22) (2019) 3074–3080.

[40] J.D. Goodpaster, A.T. Bell, M. Head-Gordon, Identification of possible pathways for C–C bond formation during electrochemical reduction of CO2: New theoretical insights from an improved electrochemical model, J. Phys. Chem. Lett. 7 (8) (2016) 1471–1477, PMID: 27045040.

[41] S. Goedecker, Linear scaling electronic structure methods, Rev. Modern Phys. 71 (1999) 1085–1123.

[42] M.M. Melander, M.J. Kuisma, T.E.K. Christensen, K. Honkala, Grand-canonical approach to density functional theory of electrocatalytic systems: Thermodynamics of solid-liquid interfaces at constant ion and electrode potentials, J. Chem. Phys. 150 (4) (2019) 041706.

[43] K. Letchworth-Weaver, T.A. Arias, Joint density functional theory of the electrode-electrolyte interface: Application to fixed electrode potentials, interfacial capacitances, and potentials of zero charge, Phys. Rev. B 86 (2012) 075140.

[44] R. Sundararaman, W.A. Goddard, T.A. Arias, Grand canonical electronic density-functional theory: Algorithms and applications to electrochemistry, J. Chem. Phys. 146 (11) (2017) 114104.

[45] A.Y. Lozovoi, A. Alavi, J. Kohanoff, R.M. Lynden-Bell, Ab initio simulation of charged slabs at constant chemical potential, J. Chem. Phys. 115 (4) (2001) 1661–1669.

[46] A.Y. Lozovoi, A. Alavi, Reconstruction of charged surfaces: General trends and a case study of Pt(110) and Au(110), Phys. Rev. B 68 (2003) 245416.

[47] S. Ringe, H. Oberhofer, K. Reuter, Transferable ionic parameters for first-principles Poisson-Boltzmann solvation calculations: Neutral solutes in aqueous monovalent salt solutions, J. Chem. Phys. 146 (13) (2017) 134103.

[48] O. Andreussi, I. Dabo, N. Marzari, Revised self-consistent continuum solvation in electronic-structure calculations, J. Chem. Phys. 136 (6) (2012) 064102.

[49] J. Dziedzic, H.H. Helal, C.-K. Skylaris, A.A. Mostofi, M.C. Payne, Minimal parameter implicit solvent model for ab initio electronic-structure calculations, EPL (Europhys. Lett.) 95 (4) (2011) 43001.

[50] N. Lespes, J.-S. Filhol, Using implicit solvent in ab initio electrochemical modeling: investigating Li+/Li electrochemistry at a Li/solvent interface, J. Chem. Theory Comput. 11 (7) (2015) 3375–3382.

[51] S.E. Weitzner, T.A. Pham, C.A. Orme, S.R. Qiu, B.C. Wood, Beyond thermodynamics: Assessing the dynamical softness of hydrated ions from first principles, J. Phys. Chem. Lett. 12 (49) (2021) 11980–11986.

[52] J. Gray, B. El Dasher, C. Orme, Competitive effects of metal dissolution and passivation modulated by surface structure: An AFM and EBSD study of the corrosion of alloy 22, Surf. Sci. 600 (12) (2006) 2488–2494.

[53] R.A. Marcus, On the theory of oxidation-reduction reactions involving electron transfer. I, J. Chem. Phys. 24 (5) (1956) 966–978.

[54] R.A. Marcus, On the theory of electron-transfer reactions. VI. Unified treatment for homogeneous and electrode reactions, J. Chem. Phys. 43 (2) (1965) 679–701.

[55] G.S. Hammond, A correlation of reaction rates, J. Am. Chem. Soc. 77 (2) (1955) 334–338.

[56] D.I. Oyarzun, C. Zhan, S.A. Hawks, M.R. Cerón, H.A. Kuo, C.K. Loeb, F. Aydin, T.A. Pham, M. Stadermann, P.G. Campbell, Unraveling the ion adsorption kinetics in microporous carbon electrodes: A multiscale quantum-continuum simulation and experimental approach, ACS Appl. Mater. Interfaces 13 (20) (2021) 23567–23574.

[57] A.J. Cohen, P. Mori-Sánchez, W. Yang, Insights into current limitations of density functional theory, Science 321 (5890) (2008) 792–794.